Computers and Structures 142 (2014) 1–14

Contents lists available at ScienceDirect

Computers and Structures

journal homepage: www.elsevier.com/locate/compstruc

The method of finite spheres for wave propagation problems

Seounghyun Ham, Benjamin Lai, Klaus-Jürgen Bathe *

Massachusetts Institute of Technology, Cambridge, MA 02139, United States

ARTICLE INFO

Article history:
Received 26 March 2014
Accepted 27 May 2014

Keywords:
Method of finite spheres
Meshless method
Wave propagation
Harmonic functions
Numerical integration
Implicit time integration

ABSTRACT

We present in this paper the development and use of a novel and promising numerical scheme, the method of finite spheres, for the analysis of wave propagations. The solution of two-dimensional linear elastic and visco-elastic waves is considered. The procedure does not require a mesh and hence avoids element distortions. We discuss the construction of the interpolations in which harmonic functions are included to make the method effective for the analysis of wave propagations. A simple and efficient numerical integration scheme is proposed and the solution effort is evaluated versus using the standard finite element method. Several numerical examples are used to demonstrate capabilities of the method.

1. Introduction

The objective in the development of the method of finite spheres is to obtain a reliable and efficient method to solve complex boundary value problems without the construction of a mesh [1–6]. The method was developed during a period of increasing awareness and promise of meshless methods with the aim to overcome some inherent limitations of numerical methods that rely on the use of a mesh [7]. The finite element method requires the discretization of a problem domain into a set of non-overlapping elements. The consequence of a poorly constructed discretization can be a significant loss in accuracy of the solution [8]. In addition, for wave propagation problems, the standard finite element method may not be effective since very fine meshes are required and even when using such fine meshes the solution may still show significant spurious oscillations, and dispersion and dissipation errors. The enriched finite element method using an implicit time integration scheme was developed to address these difficulties [9–11]. However, measured on the experiences obtained, there is still significant need for improved solution procedures.

Several other methods have been proposed for the solution of wave propagation problems [12–32]. The spectral element method is a high-order Lagrangian-based finite element technique that combines the approach of using finite elements with the accuracy of spectral methods. Lagrange polynomials approximate the field variables and Gauss–Lobatto quadrature is used for the required integrations leading to a diagonal mass matrix when using quadrilateral or hexahedral elements in two- and three-dimensional solutions, respectively, which is advantageous for the analysis of transient wave propagation problems [13–15]. The major difficulty, however, is to mesh complex two- and three-dimensional domains and obtain effective solutions using a mixture of elements.

Meshless methods have attracted significant attention for the analyst to solve boundary value problems without the use of a predefined mesh. Some meshless procedures have also been developed for the solution of wave propagation problems and can generally be categorized into strong-form and weak-form methods. Smoothed particle hydrodynamics (SPH) is a well-known strong-form method, initially used for modeling astrophysical phenomena [16,17]. Weak-form methods include the element-free Galerkin method (EFG) [18,19], the meshless local Petrov–Galerkin method (MLPG) [20–23], and the method of finite spheres (MFS) [1]. Meshless methods can also be categorized by their choice of interpolation functions. For example, methods employing radial basis functions (RBF) have been developed for the solution of transient acoustic wave propagation problems [24–26].

The SPH scheme is a commonly used method for simulating fluids. The method represents the field quantity in an integral form based on kernel approximation functions. Current research has also illustrated the applicability of SPH for the solution of wave propagation problems in solid mechanics. The major difficulties commonly cited for SPH are tensile instability and boundary deficiency [16,17]. Tensile instability refers to an unstable solution when tensile stresses are present. Boundary deficiency is a consequence of not satisfying zeroth-order consistency near or on the boundary of the problem domain. Improvements addressing these

* Corresponding author. Tel.: +1 6179265199.
E-mail address: kjb@mit.edu (K. J. Bathe).

http://dx.doi.org/10.1016/j.compstruc.2014.05.012
0045-7949/

difficulties have been developed and the improved schemes were shown to provide good accuracy for the solution of shock wave propagations in viscoplastic media [17]. However, the SPH scheme still requires the use of a large number of nodes to obtain reasonably accurate solutions and the use of some 'adjustable solution factors' that render the method not applicable, for example, to the solution of simple linear elastic static problems.

The element-free Galerkin method has been shown to provide good results for acoustic and elastic wave propagation problems [19]. Imposing the Dirichlet boundary conditions, however, is not straightforward since the interpolation functions do not satisfy the Kronecker delta property. Lagrange multipliers can be used, but this leads to a larger system of algebraic equations and a loss of positive definiteness which reduces the computational efficiency. Alternatively, the penalty method can be employed, but then appropriate penalty factors need to be chosen, that may depend on the problem considered [18,19].

The meshless local Petrov–Galerkin method adopts trial and test functions from different approximation spaces, resulting in various formulations [20–23]. The MLPG approach has been used to solve for the propagation and scattering of electromagnetic waves, where the trial functions are constructed from moving least squares approximations and the test functions from solutions of Green's problem [22]. The method has also been used for the solution of wave propagations in three-dimensional poroelastic solids, with the trial functions constructed using radial basis functions and the test functions being simply unit step functions [23]. While the given numerical solutions are in good agreement with analytical solutions, these methods are computationally expensive due to the non-symmetry of the coefficient matrices and the numerical integration of complex expressions within the subdomains.

The method of finite spheres is related to the above techniques in that it is based on a weak formulation of boundary value problems using overlapping subdomains, and hence also does not require a mesh. In fact, the only difference to the standard finite element method is that the spheres (subdomains, or elements) overlap, and indeed other subdomains (like bricks) could be employed. The method is using symmetric coefficient matrices and was initially presented for the analysis of linear static solids and fluids [1]. Further research focused on the method of finite spheres in a mixed formulation, improved numerical integration, automatic discretization, coupling with the finite element method, and enrichment strategies [2–6]. In this paper, we seek to demonstrate that there is significant promise of reliability and efficiency for the method of finite spheres in the solution of wave propagation problems.

We briefly review the method of finite spheres in Section 2. We give the interpolation functions used for general elliptic problems and introduce the special interpolation functions used for wave propagation problems. In Section 3, the formulation for the analysis of two-dimensional linear elastic wave propagation problems is presented. Since efficiency is a particular concern for the use of the method of finite spheres, a simple improved numerical integration scheme is given in Section 4. Finally, to illustrate the capabilities of the developed scheme, we present in Section 5 the results of several wave propagation problems in elastic and visco-elastic media.

Since we consider in this paper only the solution of two-dimensional problems, we should note that when referring to a "sphere", a "disk" is implied.

2. Interpolation scheme

The method of finite spheres uses the Shepard partition of unity functions. The interpolations are defined by the Shepard functions times local basis functions that can include any desired enrichments [1]. Consistency and continuity conditions are satisfied by proper selection of the local basis functions that together span the local approximation space. Computational efficiency depends on the suitability of these functions when considering the degree of the governing partial differential equations and the nature of the solutions to be predicted.

2.1. Shepard partition of unity functions

Let $V \in R^d (d = 1, 2, or\ 3)$ be an open bounded domain and let S be the domain boundary, with $S = S_u \cup S_f$ and $S_u \cap S_f = 0$, where S_u is the Dirichlet boundary and S_f is the Neumann boundary. Then let $\{B(\underline{x}_I, r_I);\ I = 1, 2, \ldots, N\}$ be a set of spheres which form a covering for V, i.e., $V \subset \bigcup_{I=1}^{N} B(\underline{x}_I, r_I)$, where $\underline{x}_I$ and r_I refer to the center and radius of the sphere B_I, respectively, and where I is the nodal label of each sphere and N is the total number of spheres. The unit normal to the domain boundary, $\underline{n}$, is positive in the outward direction. As illustrated in Fig. 1, spheres are either interior spheres, entirely within the problem domain, or boundary spheres intercepting the domain boundary.

Let $W_I(\underline{x})$ denote a positive radial weighting function of the form $W_I(\underline{x}) = W(s_I)$, with $s_I = ||\underline{x} - \underline{x}_I||/r_I$ where $||\cdot||$ is the Euclidean norm. We use the quartic spline weighting function defined as

$$W(s_I) = \begin{cases} 1 - 6s_I^2 + 8s_I^3 - 3s_I^4, & 0 \leqslant s_I \leqslant 1 \\ 0, & s_I > 1 \end{cases} \tag{1}$$

The Shepard partition of unity function is then given by

$$\varphi_I^0(\underline{x}) = \frac{W_I}{\sum_{J=1}^{N} W_J}, \quad I = 1, 2, \ldots, N \tag{2}$$

Hence $\sum_{I=1}^{N} \varphi_I^0(\underline{x}) = 1\ \forall \underline{x} \in V$. These functions are rational, non-polynomial functions satisfying zeroth order consistency, ensuring that rigid body modes can be reproduced exactly.

To generate approximation spaces of higher order consistency, a local approximation space $V_I^h = \text{span}_{m \in \mathcal{J}}\{p_m(\underline{x})\}$ is defined at each node I, where h is a measure of the sphere size, $\mathcal{J}$ is an index set, and $p_m(\underline{x})$ is a member of the local basis. Then the global approximation space V_h is defined as the product of the Shepard function at each node I and the functions from the local bases

$$V_h = \sum_{I=1}^{N} \varphi_I^0 V_I^h \tag{3}$$

Hence any function v_h in the solution space V_h can be written as

$$v_h(\underline{x}) = \sum_{I=1}^{N} \sum_{m \in \mathcal{J}} h_{Im}(\underline{x}) \alpha_{Im} \tag{4}$$

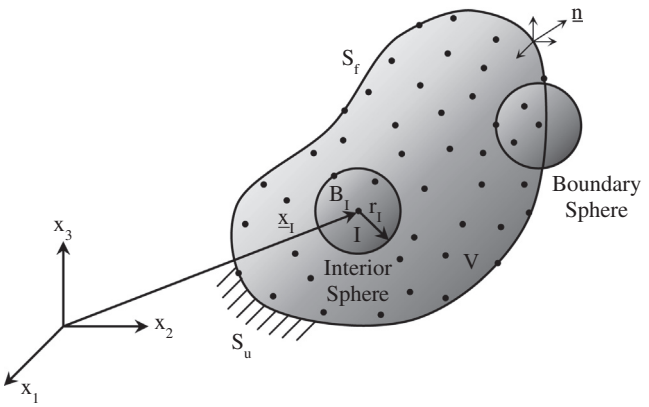

Fig. 1. General problem domain V with domain boundary $S = S_u \cup S_f$.

with the interpolation functions

$$h_{Im}(\underline{x}) = \varphi_I^0(\underline{x}) p_m(\underline{x}) \tag{5}$$

and the mth degree of freedom α_{Im} at node I. Hence, the number of degrees of freedom depends on the number of functions included in the local approximation space. Furthermore, depending on the nature of the solutions, the optimal choice of the members of the local basis can improve the accuracy and efficiency of the solution.

An important point pertaining to the method of finite spheres is that we are able to choose effective functions for solving specific problems, unlike done in the standard finite element method. The nature of the solutions is distinctly different for different categories of problems [8] and so it is natural to employ different interpolation functions for different classes of problems.

2.2. Interpolation functions for elliptic problems

For the solution of elliptic problems [8], a suitable local approximation space defined in two dimensions is

$$V_I^h = \text{span}\{1, x, y, x^2, xy, y^2\} \tag{6}$$

containing the terms of a complete second order polynomial. Fig. 2 shows the one-dimensional interpolation functions for elliptic problems.

2.3. Interpolation functions for hyperbolic problems

For the solution of two-dimensional hyperbolic problems, a suitable local approximation space is [9]

$$V_I^h = \text{span}\left\{\begin{matrix} 1, x, y, xy, \\ \cos\left(\frac{2\pi k_x x}{\Lambda_x}\right), \sin\left(\frac{2\pi k_x x}{\Lambda_x}\right), \cos\left(\frac{2\pi k_y y}{\Lambda_y}\right), \sin\left(\frac{2\pi k_y y}{\Lambda_y}\right), \\ \cos\left(\frac{2\pi k_x x}{\Lambda_x} \pm \frac{2\pi k_y y}{\Lambda_y}\right), \sin\left(\frac{2\pi k_x x}{\Lambda_x} \pm \frac{2\pi k_y y}{\Lambda_y}\right) \end{matrix}\right\}, \begin{matrix} k_x, k_y = 1, \ldots, p \\ p \in \{1, 2, 3\} \end{matrix} \tag{7}$$

where Λ_x and Λ_y are fundamental wavelengths in the x- and y-directions, respectively, k_x and k_y are integers from $1, \ldots, p$, and p is the cutoff number. A suitable choice for the fundamental wavelengths is $\Lambda_x = \Lambda_y = 2r_I$ [9]. Higher-order trigonometric functions are included as the cutoff number increases, but the condition number of the constructed matrices increases as additional terms are included, hence an upper bound of $p = 3$ has been selected. Fig. 3 shows the one-dimensional interpolation functions with cutoff number $p = 1$ for hyperbolic problems. We note that with this choice of basis functions, the scheme satisfies the patch tests [8].

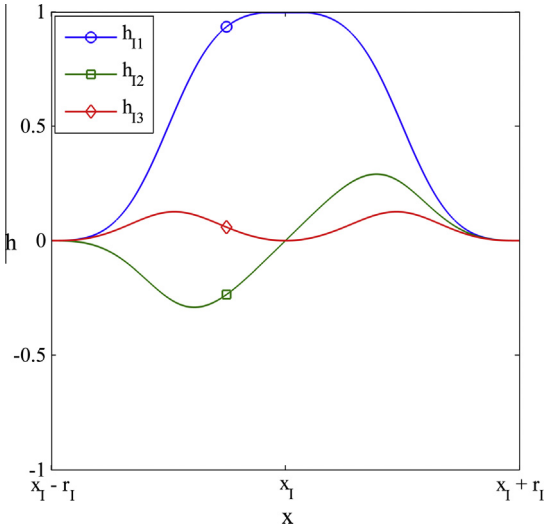

Fig. 2. One-dimensional interpolation functions for elliptic problems $h_{I1} = \varphi_I^0$, $h_{I2} = \varphi_I^0 x$, $h_{I3} = \varphi_I^0 x^2$.

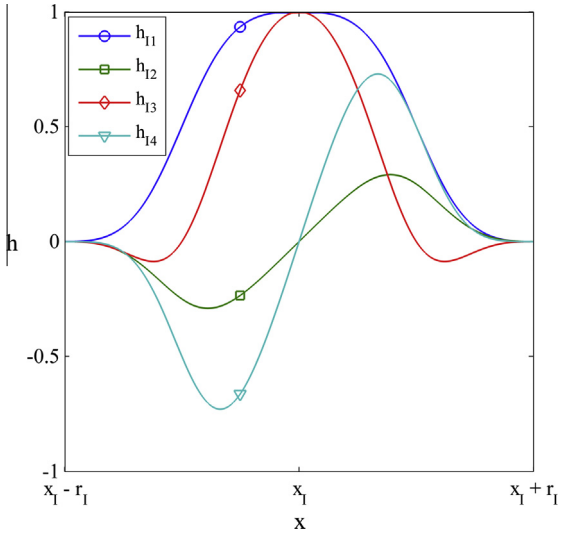

Fig. 3. One-dimensional interpolation functions with $p = 1$ for hyperbolic problems $h_{I1} = \varphi_I^0$, $h_{I2} = \varphi_I^0 x$, $h_{I3} = \varphi_I^0 \cos\left(\frac{2\pi x}{\Lambda_x}\right)$, $h_{I4} = \varphi_I^0 \sin\left(\frac{2\pi x}{\Lambda_x}\right)$.

3. Two-dimensional wave propagation

In this section we apply the framework of the method of finite spheres to solve two-dimensional wave propagation problems using the displacement-based formulation of the method of finite spheres.

3.1. Governing differential equations

The governing differential equations for a linear elastic domain $V \in R^2$ with boundary S are

$$\underline{\partial}_\varepsilon^T \underline{\tau} + \underline{f}^B = \underline{0} \text{ in } V \tag{8}$$

with Neumann boundary conditions

$$\underline{N}\underline{\tau} = \underline{f}^S \text{ on } S_f \tag{9}$$

and Dirichlet boundary conditions

$$\underline{u} = \underline{u}^S \text{ on } S_u \tag{10}$$

The strain–displacement relation is

$$\underline{\varepsilon} = \underline{\partial}_\varepsilon \underline{u} \tag{11}$$

and the linear elastic constitutive relation is

$$\underline{\tau} = \underline{C}\underline{\varepsilon} \tag{12}$$

In Eqs. (8)–(12), $\underline{u}$, $\underline{\varepsilon}$, and $\underline{\tau}$ are the displacement, strain, and stress vectors, respectively, $\underline{f}^B$ is the body force vector (including inertia terms), $\underline{f}^S$ is the prescribed traction vector, $\underline{u}^S$ is the prescribed displacement vector, $\underline{\partial}_\varepsilon$ is a linear gradient operator, $\underline{N}$ is the direction cosine matrix for the unit normal to the domain boundary (positive outwards), and $\underline{C}$ is the elasticity matrix.

3.2. Variational formulation

For the linear elastic domain $V \in R^2$, the variational indicator is

$$\Pi(\underline{u}) = \frac{1}{2}\int_V \underline{\varepsilon}^T(\underline{u})\underline{C}\underline{\varepsilon}(\underline{u})dV - \int_V \underline{u}^T(\underline{\hat{f}}^B - \rho\underline{\ddot{u}})dV - \int_{S_f} \underline{u}^T\underline{f}^S dS - \int_{S_u} \underline{f}^{uT}(\underline{u} - \underline{u}^S)dS \tag{13}$$

where $\hat{\underline{f}}^B$ does not include inertia forces, ρ is the mass density, $\ddot{\underline{u}}$ is the acceleration vector, and $\underline{f}^u = \underline{NC\varepsilon}(\underline{u})$ is the traction vector on the Dirichlet boundary. Invoking the stationarity of the given variational indicator Π, we obtain the following weak form:

Find $\underline{u} \in H^1(V)$ such that

$$\int_V \underline{\varepsilon}^T(\underline{v})\underline{C\varepsilon}(\underline{u})dV + \int_V \underline{v}^T\rho\ddot{\underline{u}}dV - \int_{S_u}[\underline{\varepsilon}^T(\underline{v})\underline{CN}^T\underline{u} + \underline{v}^T\underline{NC\varepsilon}(\underline{u})]dS = \int_V \underline{v}^T\hat{\underline{f}}^B dV + \int_{S_f}\underline{v}^T\underline{f}^S dS - \int_{S_u}\underline{\varepsilon}^T(\underline{v})\underline{CN}^T\underline{u}^S dS \;\forall \underline{v} \in H^1(V) \quad (14)$$

where $H^1(V)$ is the first-order Hilbert space [8].

3.3. Nodal interpolations

For two-dimensional analysis, the displacement field approximation is

$$\underline{u}(x,y) = \begin{Bmatrix} u(x,y) \\ v(x,y) \end{Bmatrix} = \sum_{J=1}^{N}\sum_{n\in\mathcal{J}} \underline{H}_{Jn}(x,y)\underline{\alpha}_{Jn} = \underline{H}(x,y)\underline{U} \quad (15)$$

The corresponding strain field is

$$\underline{\varepsilon}(x,y) = \begin{Bmatrix} \varepsilon_{xx} \\ \varepsilon_{yy} \\ \gamma_{xy} \end{Bmatrix} = \sum_{J=1}^{N}\sum_{n\in\mathcal{J}} \underline{B}_{Jn}(x,y)\underline{\alpha}_{Jn} = \underline{B}(x,y)\underline{U} \quad (16)$$

and the stress field is hence

$$\underline{\tau}(x,y) = \begin{Bmatrix} \tau_{xx} \\ \tau_{yy} \\ \tau_{xy} \end{Bmatrix} = \sum_{J=1}^{N}\sum_{n\in\mathcal{J}} \underline{CB}_{Jn}(x,y)\underline{\alpha}_{Jn} = \underline{CB}(x,y)\underline{U} \quad (17)$$

where $\underline{\alpha}_{Jn} = \begin{bmatrix} u^{Jn} & v^{Jn} \end{bmatrix}$ is the vector of nodal unknowns at node J corresponding to the nth degree of freedom, u^{Jn} and v^{Jn} are the x- and y-direction displacements, respectively, at node J corresponding to the nth degree of freedom, and $\underline{U} = [\,\underline{\alpha}_{11} \quad \underline{\alpha}_{12} \quad \underline{\alpha}_{13} \cdots \underline{\alpha}_{Jn} \cdots]^T$ is the vector of nodal unknowns.

In the above equations we have

$$\underline{H}_{Jn}(x,y) = \begin{bmatrix} h_{Jn}(x,y) & 0 \\ 0 & h_{Jn}(x,y) \end{bmatrix} \quad (18)$$

$$\underline{B}_{Jn}(x,y) = \underline{\partial_\varepsilon}\underline{H}_{Jn}(x,y) = \begin{bmatrix} \partial h_{Jn}/\partial x & 0 \\ 0 & \partial h_{Jn}/\partial y \\ \partial h_{Jn}/\partial y & \partial h_{Jn}/\partial x \end{bmatrix} \quad (19)$$

and the elasticity matrix

$$\underline{C} = \begin{bmatrix} c_{11} & c_{12} & 0 \\ c_{12} & c_{11} & 0 \\ 0 & 0 & c_{33} \end{bmatrix} \quad (20)$$

where for plane stress conditions,

$$c_{11} = \frac{E}{1-\nu^2}, \quad c_{12} = \frac{E\nu}{1-\nu^2} \quad c_{33} = \frac{E}{2(1+\nu)}$$

and for plane strain conditions,

$$c_{11} = \frac{E(1-\nu)}{(1+\nu)(1-2\nu)}, \quad c_{12} = \frac{E\nu}{(1+\nu)(1-2\nu)}, \quad c_{33} = \frac{E}{2(1+\nu)}$$

with E and ν being Young's modulus and Poisson's ratio of the material, respectively.

3.4. Discrete equations

Substituting Eqs. (15)–(17) into Eq. (14), the discretized system of algebraic equations corresponding to node I and degree of freedom m is

$$\sum_{J=1}^{N}\sum_{n\in\mathcal{J}} \underline{M}_{ImJn}\ddot{\underline{\alpha}}_{Jn} + \sum_{J=1}^{N}\sum_{n\in\mathcal{J}} \underline{K}_{ImJn}\underline{\alpha}_{Jn} = \underline{f}_{Im} + \hat{\underline{f}}_{Im} \quad (21)$$

where the mass matrix is

$$\underline{M}_{ImJn} = \int_{V_I} \underline{H}_{Im}\rho\underline{H}_{Jn}dV \quad (22)$$

the stiffness matrix is

$$\underline{K}_{ImJn} = \int_{V_I} \underline{B}_{Im}^T\underline{CB}_{Jn}dV \quad (23)$$

and the body force load vector is

$$\underline{f}_{Im} = \int_{V_I} \underline{H}_{Im}\hat{\underline{f}}^B dV \quad (24)$$

with $V_I = V \cap B(\underline{x}_I, r_I)$.

The traction force vector corresponding to node I and degree of freedom m is

$$\hat{\underline{f}}_{Im} = \begin{cases} \underline{0}, & \text{for an interior sphere} \\ \int_{S_{f_I}} \underline{H}_{Im}\underline{f}^S dS, & \text{for a Neumann boundary sphere} \\ \sum_{J=1}^{N}\sum_{n\in\mathcal{J}} \underline{KU}_{ImJn}\underline{\alpha}_{Jn} - \underline{fU}_{Im}, & \text{for a Dirichlet boundary sphere} \end{cases} \quad (25)$$

where

$$\underline{KU}_{ImJn} = \int_{S_{u_I}} \underline{H}_{Im}\underline{NCB}_{Jn}dS + \int_{S_{u_I}} \underline{B}_{Im}^T\underline{CN}^T\underline{H}_{Jn}dS \quad (26)$$

and

$$\underline{fU}_{Im} = \int_{S_{u_I}} \underline{B}_{Im}^T\underline{CN}^T\underline{u}^S dS \quad (27)$$

with $S_f = \bigcup_{I\in N_f} S_{f_I}$, N_f = index set of nodes with nonzero intercept on the Neumann boundary and $S_u = \bigcup_{I\in N_u} S_{u_I}$, N_u = index set of nodes with nonzero intercept on the Dirichlet boundary.

4. Integration scheme

Numerical integration is a focal point of development for the method of finite spheres and in general for meshless methods [3,33,34]. In the finite element method, numerical integration is efficient due to polynomial interpolation functions, non-overlapping elements, and Gauss–Legendre product rules used over the finite element domains. The method of finite spheres requires integration of nonpolynomial functions over complicated integration domains, namely spheres, truncated spheres, and general lens-shaped regions for the overlap of spheres. Specialized integration schemes have been developed such as the piecewise midpoint quadrature rule [3]. In this research we use a simple and quite efficient procedure.

4.1. Piecewise Gauss–Legendre quadrature

For the integration, we divide the domain of each sphere (here disk) into four quadrants, as shown in Fig. 4. Within each of these quadrants, the usual Gauss–Legendre quadrature rule (the same as in standard finite element analysis [8]) is used with the objective of achieving a reasonably accurate solution using a minimal number

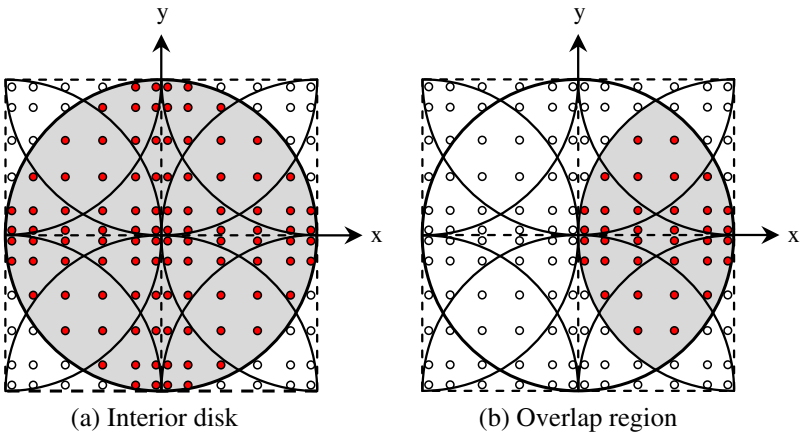

Fig. 4. Integration points for an interior sphere.

of integration points. Instead of considering different quadrature rules for different regions, simply the same rule is used for all regions in a quadrant. The advantages are that we have a uniform density of integration points and that the overlap regions are integrated directly.

This quadrature rule is very simple, and different from other schemes where isoparametric mapping is performed or different rules are used for different parts of the domains [3,5,20].

4.2. Interior disk

Considering the four quadrants, Fig. 4a, only the integration points within the disk will contribute to the evaluation of the matrices and vectors. Similarly, Fig. 4b shows the integration points used to evaluate the contributions of the lens-shaped region of overlap.

4.3. Boundary sectors

For these sectors, also no special scheme is used but simply the same integration stations used otherwise are also employed. Fig. 5a gives the integration points used within a boundary sector and Fig. 5b shows the integration points for the lens-shaped region of overlap. In each case, as above, only the integration stations within the regions considered contribute to the evaluations of the element matrices and vectors.

5. Numerical examples

The objective of this section is to demonstrate the potential of the method of finite spheres for the solution of wave propagation problems. The examples demonstrate novel features of the method of finite spheres, namely the use of interpolations enriched by trigonometric functions as well as the use of the piecewise Gauss–Legendre quadrature rule for the numerical integration.

5.1. Scalar wave

The scalar wave equation with a Ricker wavelet source at the origin is given by

$$\ddot{u}(\underline{x},t) - c^2\nabla^2 u(\underline{x},t) = F(\underline{0},t) \text{ in } V_T = V \times I \tag{28}$$

with

$$F(\underline{0},t) = 10[1 - 2\pi^2 f^2 (t-t_0)^2]\exp[-\pi^2 f^2 (t-t_0)^2] \tag{29}$$

and initial conditions

$$u(\underline{x},0) = \dot{u}(\underline{x},0) = 0 \text{ in } V \tag{30}$$

where u is the unknown displacement, c is the wave velocity, f is the peak frequency, and t_0 is the time shift. In this example, $c = 1$ m/s, $f = 6$ Hz, and $t_0 = 0.25$ s. We consider the domain $V = [0,1]\times[0,1]$, see Fig. 6, with appropriate symmetry boundary conditions, and the time domain of interest is $I = [0, 0.95\text{ s}]$.

For the solution of the transient scalar wave, the Bathe time integration method is used since it provides more accurate solutions for wave propagation problems than the trapezoidal rule [11]. The time step $\Delta t = 0.003125$ s was used. Fig. 6 gives the wave response at $t = 0.95$ s for different combinations of cutoff number and sphere size, where Fig. 6d compares these approximate solutions to the analytical solution along the x-axis. The numerical results are satisfactory. We use this example to further investigate the accuracy of the method as a function of the spatial and temporal discretizations.

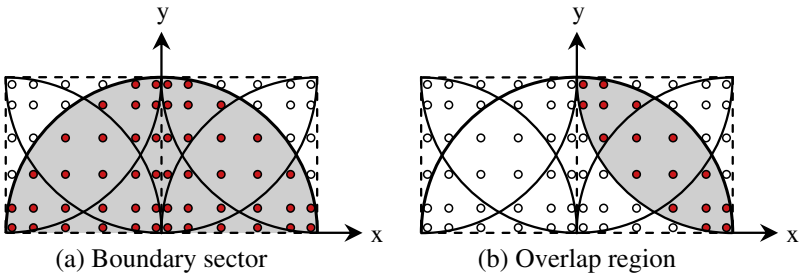

Fig. 5. Integration points for a boundary sphere.

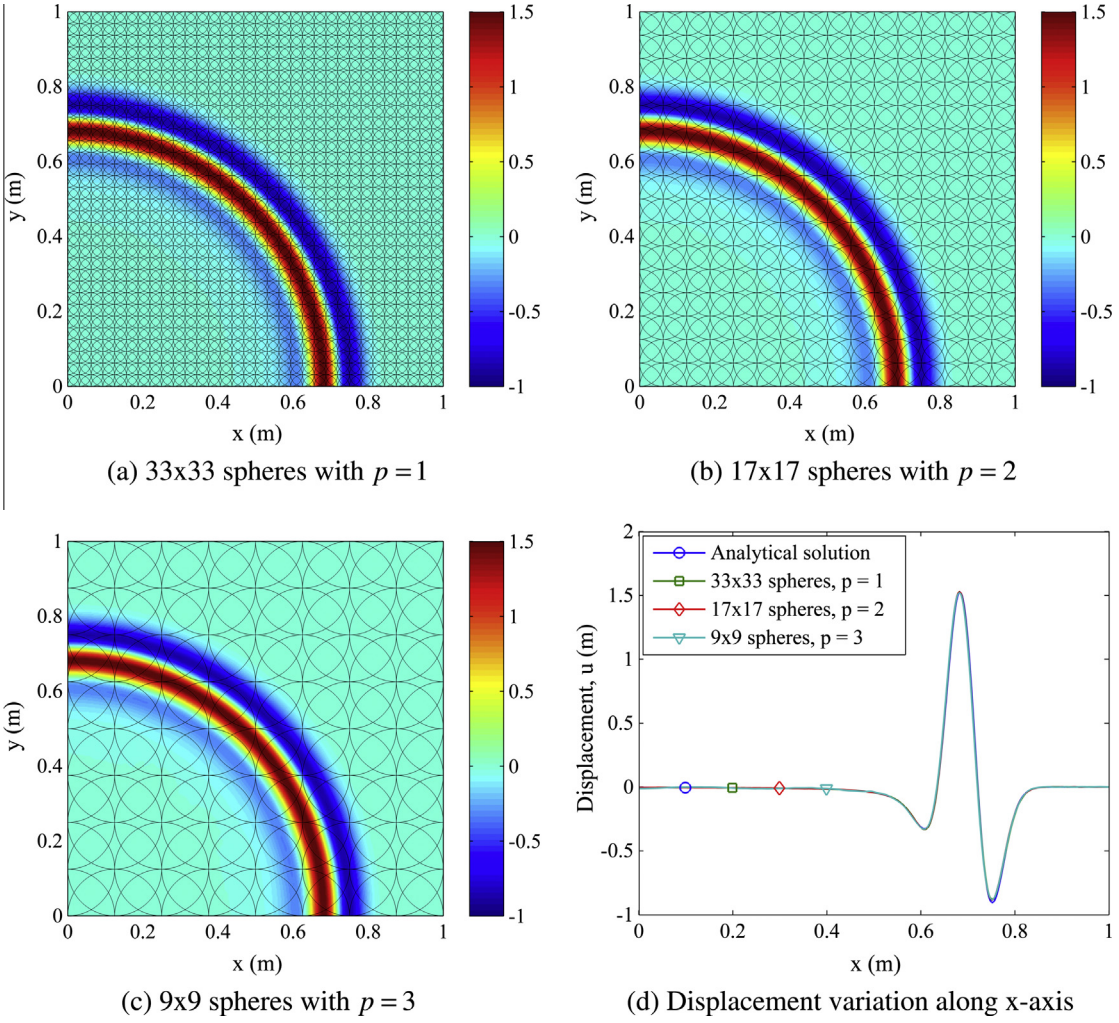

Fig. 6. Displacement contours at $t = 0.95$ s and comparison between analytical and numerical solutions.

5.1.1. Spatial and temporal discretizations

Numerical inaccuracies are usually a consequence of the spatial and temporal discretizations [8,11,35–37]. In order to minimize the spatial discretization error in the method of finite spheres, the sphere size can be decreased or the cutoff number increased, similar to h- and p-refinements, respectively, in the finite element method [8,27]. To examine h- and p-convergence of the method of finite spheres, we use the percent relative error in the L^2-norm

$$\delta = \sqrt{\frac{\int_V |u-u_h|^2 dV}{\int_V |u|^2 dV}} \times 100 \tag{31}$$

where u is the analytical solution and u_h is the numerical solution. The value of δ is quite a severe measure for wave propagation problems, because any small dispersion error can result in a large value of δ. Nevertheless we use this measure in our comparative studies. In engineering practice a less severe measure might be used. Fig. 7 shows the h- and p-convergence behavior of the method of finite spheres at $t = 0.95$ s for the scalar wave, always using $\Delta t = 0.003125$ s. As expected, the percent relative error in the L^2-norm decreases for decreasing sphere radius, and for increasing cutoff number. The remaining error of about 3% is due to the time discretization.

5.1.2. Time step size

Spatial and temporal discretizations are related by the wave speed. In order to estimate the numerical dispersion as a function of the CFL number, a deeper analysis as given in Ref. [11] should be performed. However, in the first instance we may simply use the approach given in Ref. [8]. If the critical wavelength is L_w, then the time it takes for the wave to travel this distance is

$$t_w = \frac{L_w}{c} \tag{32}$$

If n steps are required to approximate the traveling wave accurately, the appropriate time step size for the traveling wave is

$$\Delta t = \frac{t_w}{n} \tag{33}$$

The smallest wavelength that the method of finite spheres can approximate accurately is $\lambda_p = 2r_I/p$, where r_I is the radius of the sphere centered at node I and p is the cutoff number. We assume that the critical wavelength is $L_w = \lambda_p$, so the time step size is

$$\Delta t = \frac{t_w}{n} = \frac{L_w}{cn} = \frac{2r_I}{pcn} \tag{34}$$

Assuming that the smallest wavelength to be represented is based on an estimate, a reasonable value to use in practice [8] might be

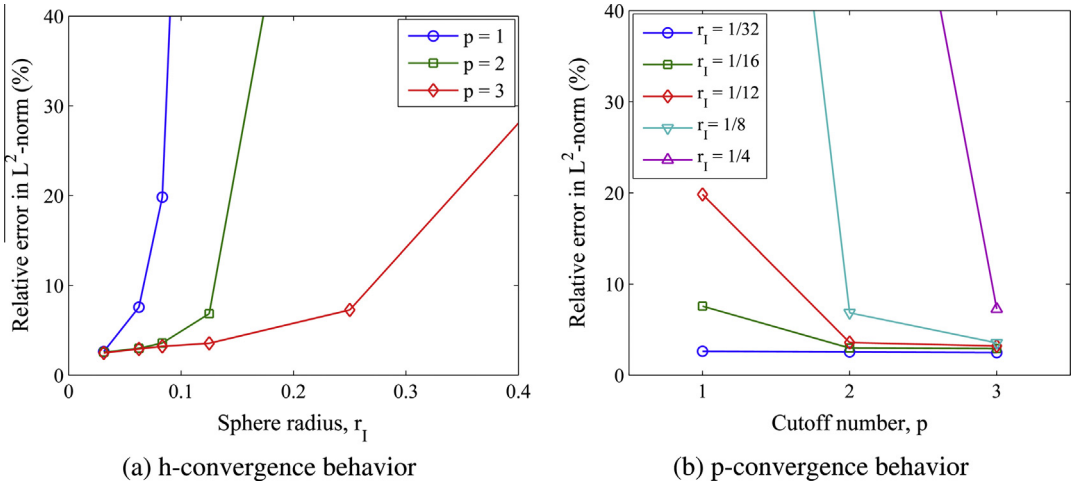

Fig. 7. Convergence behavior at $t = 0.95$ s.

$n = 6$, but we have used a larger value in our numerical experiments to obtain very accurate solutions.

Using this formula, the time step $\Delta t = 0.003125$ s used in Section 5.1.1 corresponds to the value of $n = 20$ for the discretization of 33×33 spheres with $p = 1$. This value of n is large but we have found that with $n = 20$, the error is always relatively small in the severe error measure using the L^2-norm given in Eq. (31).

5.1.3. Computational cost

The computational times used to obtain the scalar wave results shown in Fig. 6 are given in Table 1. The percent relative error in the L^2-norm and the solution times are given for two different time step sizes for each of the three spatial discretizations. For comparison, the computational times used with the traditional finite element method and 4-node elements are given in Table 2. For each discretization, two different time step sizes based on the CFL number are used.

Comparing the solution techniques, we observed that using the method of finite spheres, a smaller time step size always resulted in a decrease in the percent relative error. However, using the traditional finite element method, there is a CFL number for optimal accuracy, which for the Bathe time integration scheme is CFL = 1.0 [11]. Using a smaller time step size results in less accuracy (see also Table 2) and a coarser discretization is in general more sensitive to such change. Considering the data in Tables 1 and 2, we see that for this problem the method of finite spheres gives as efficient a solution as the traditional finite element method.

Another advantage of the method of finite spheres is that distorted elements are not an issue, that is, such sub-domains of course do not exist. Grading is simply achieved by the use of different sphere sizes. However, in traditional finite element analyses of practical problems, distorted elements are oftentimes inevitable. The distortion ratio is defined as the ratio of the longest side length to the shortest side length of any element in the domain [8]. Considering the solution of the scalar wave problem using distorted meshes, the percent relative error in the L^2-norm is given for varying distortion ratios for two finite element discretizations in Fig. 8. As expected, the percent relative error increases significantly with increase in the distortion ratio.

5.2. Scattered waves

Here we consider problems of scattered waves due to an array of rigid circular cylinders in an infinite medium. These problems are commonly encountered in the construction of ocean structures, such as oilrigs with a number of tension-legs anchored to the bottom of the ocean. The interaction between water waves and the circular cylinders is the phenomenon of interest [38,39]. We consider the wave scattering problem for a single rigid circular cylinder and for an array of rigid circular cylinders.

Fig. 9 describes the problem when there is a single rigid circular cylinder. A plane wave traveling in the x-direction strikes the circular cylinder, and the wave scatters around and radiates away from the cylinder. The analytical solution for the scattered wave is given by

$$u(r,\theta) = -\sum_{n=0}^{\infty} i^n \rho_n \frac{J_n'(ka)}{H_n'(ka)} H_n(kr)\cos(n\theta) \tag{35}$$

where u is the wave response, r and θ are polar coordinates measured from the center of the cylinder, $\rho_n = 1$ for $n = 0$ and $\rho_n = 2$ for $n \geqslant 1$, J_n is the Bessel function, H_n is the Hankel function, $ka = 6\pi$ is the wave number, and $a = 1$ is the radius of the cylinder. Since the analytical solution consists of an infinite number of terms, we sum from $n = 0, \ldots, 20$ to obtain our reference analytical solution.

For the numerical solution, we apply the reference analytical solution to the boundary of the circular cylinder as a Dirichlet boundary condition. The radiation boundary condition to model an infinite domain is replaced by a perfectly matched layer [9,39,40]. Using either an absorbing boundary condition or a perfectly matched layer to simulate the unbounded physical domain results in some numerical errors, but here the error is negligible. The computational domain using a 21×21 discretization of

Table 1
Percent relative errors and computational times using the method of finite spheres.

Discretization	9×9, $p = 3$		17×17, $p = 2$		33×33, $p = 1$	
Time step size (s)	0.003125	0.00625	0.003125	0.00625	0.003125	0.00625
Relative error (%)	3.55	10.37	2.98	10.54	2.63	10.27
Solution time (s)	48.37	36.99	69.97	45.09	90.63	52.11

Table 2
Percent relative errors and computational times using the finite element method, 4-node elements.

Discretization	80 × 80		160 × 160	
Time step size (s)	0.00625 (CFL = 0.5)	0.0125 (CFL = 1)	0.003125 (CFL = 0.5)	0.00625 (CFL = 1)
Relative error (%)	21.26	12.73	5.59	3.27
Solution time (s)	12.32	6.13	110.06	59.75

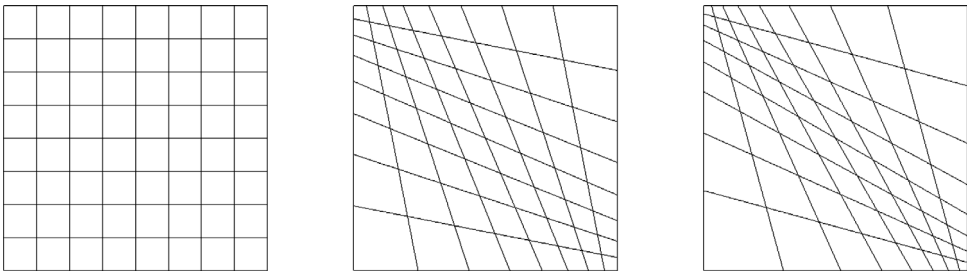

Distortion ratio = 1 Distortion ratio = 5 Distortion ratio = 10

(a) Schematic of distorted meshes used, showing 8x8 element mesh

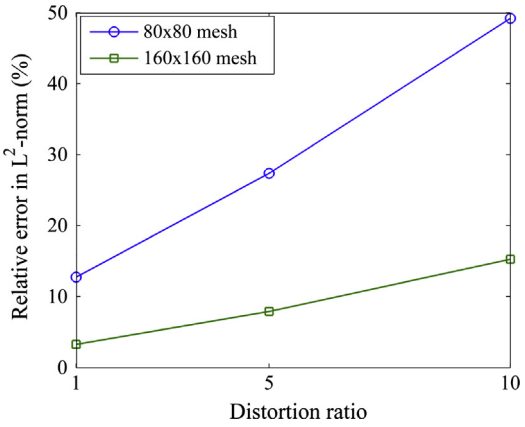

(b) Error as a function of element distortions

Fig. 8. Percent relative error in the L^2-norm as a function of distortion ratio.

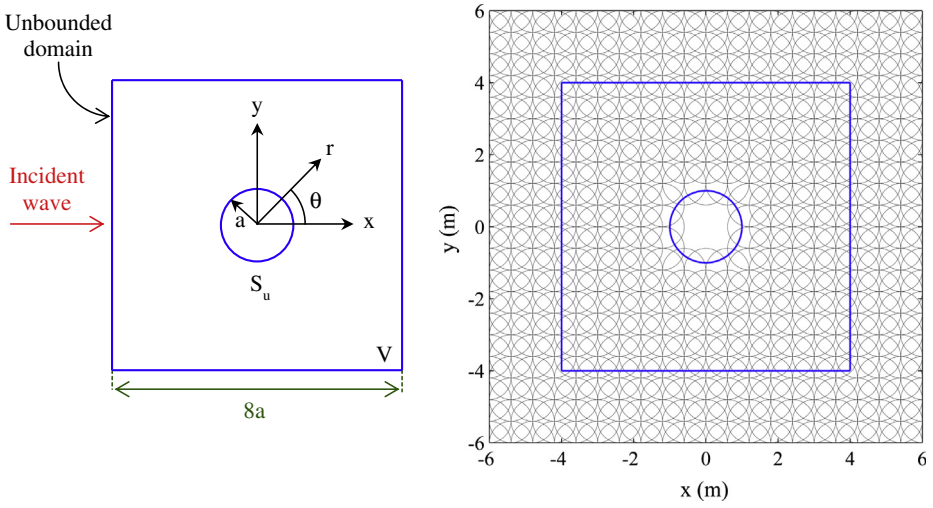

(a) Single rigid cylinder (b) 21x21 sphere discretization

Fig. 9. Problem description and discretization of the computational domain edged with a perfectly matched layer, case of 1 cylinder.

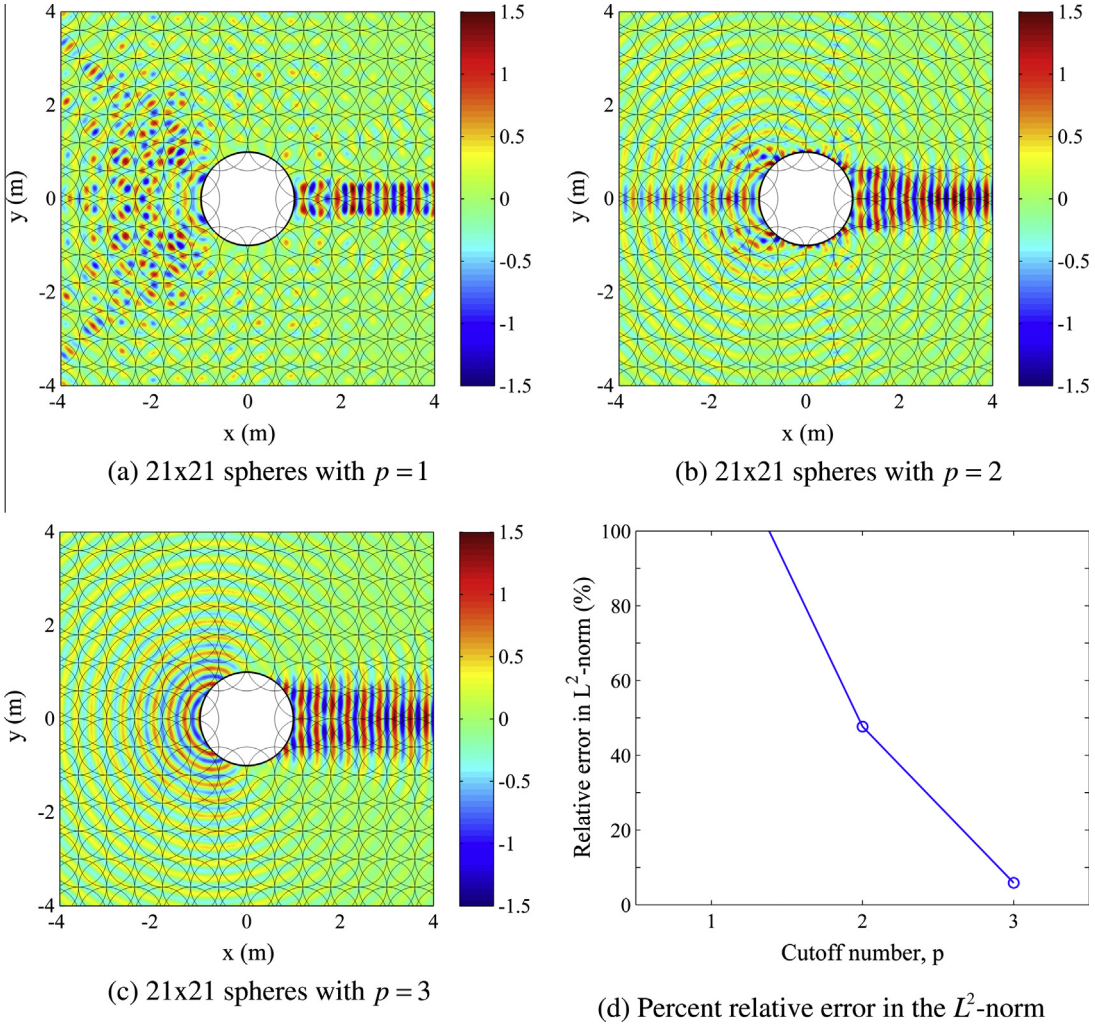

Fig. 10. Real part of numerical solution and percent relative error in the L^2-norm as a function of cutoff number.

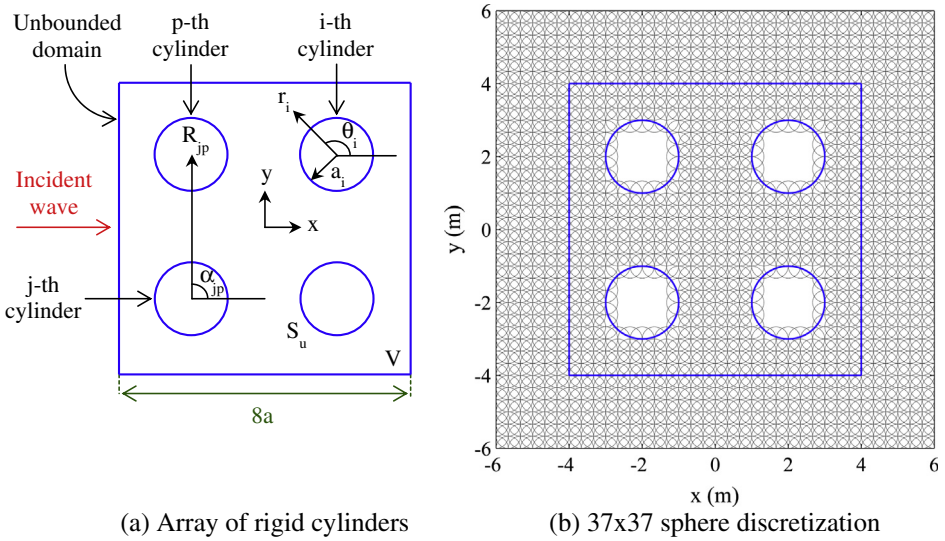

Fig. 11. Problem description and discretization of the computational domain edged with a perfectly matched layer, case of 4 cylinders.

regularly arranged spheres is shown in Fig. 9b. Fig. 10 provides plots of the real part of the scattered wave solutions using cutoff numbers $p = 1, 2, 3$. The results obtained using the cutoff number $p = 1$ show a scattered wave deterioration since the reflected wave is not completely absorbed by the perfectly matched layer, due to inadequate spatial discretization. However, the results obtained using the cutoff number $p = 3$ are in close agreement with the analytical reference solution.

Next we consider the same problem but with an array of four rigid circular cylinders, see Fig. 11. The scattered wave from one cylinder now interacts with the other cylinders, causing multiple scattering of waves. The analytical solution is given by

$$u(r,\theta) = \sum_{j=1}^{N}\sum_{q=-M}^{M} B_q^j \frac{J_q'(ka_j)}{H_q'(ka_j)} H_q(kr_j)\exp(iq\theta_j) \tag{36}$$

where the unknown coefficients B_q^j are found by solving

$$B_l^p + \sum_{j=1, j\neq p}^{N}\sum_{q=-M}^{M} B_q^j \frac{J_q'(ka_j)}{H_q'(ka_j)} \exp[i(q-l)\alpha_{jp}] H_{q-l}(kR_{jp}) = -\exp\left[i\left(kx_p + \frac{\pi}{2}l\right)\right] \tag{37}$$

with $p = 1, \ldots, N$ and $l = -M, \ldots, M$. The wave number is $ka_j = 8\pi$ and the radii of the cylinders are $a_j = a = 1$ for all j. Higher accuracy is achieved by increasing M. We used $M = 10$ for the problem reference solution [38,39].

We discretize the domain using 37×37 spheres, see Fig. 11b, and prescribe the analytical reference solution as a Dirichlet boundary condition on the boundaries of the cylinders. A perfectly matched layer is used along the edges of the domain boundary. Fig. 12 provides plots of the real part of the scattered wave solutions using cutoff numbers $p = 1, 2, 3$, where the results obtained using the cutoff number $p = 3$ are in good agreement with the analytical reference solution.

5.3. Elastic waves

In this section, we solve for the elastic waves propagating within a semi-infinite domain due to an imposed surface force. The isotropic plane strain elastic medium has P-wave velocity $v_p = 3200$ m/s, S-wave velocity $v_s = 1847.5$ m/s, and mass density $\rho = 2200$ kg/m^3. The domain size is 4000 m $\times$ 2000 m and the forcing function is a Ricker wavelet, see Eq. (29), with magnitude 10^6, frequency $f = 10$ Hz, time shift $t_0 = 0.10$ s and vertically imposed on the surface at $(x, y) = (2000\text{ m}, 2000\text{ m})$, see Fig. 13. The spatial discretization is 51×26 spheres using the cutoff number $p = 2$. The simulation duration is 1.0 s and the Bathe time integration method is used with time step size $\Delta t = 0.0008$ s. Fig. 13 shows the wave profiles at $t = 0.74$ s, where the P-, S-, and Rayleigh waves can be identified. Fig. 14 provides a comparison between the analytical and numerical solutions at two receivers, $(x_1, y_1) = (2640\text{ m}, 2000\text{ m})$ and $(x_2, y_2) = (3280\text{ m}, 2000\text{ m})$.

The Rayleigh wave traveling along the surface might be used to test whether a numerical method is capable of accurately approximating the free-surface boundary condition [14]. Fig. 14 illustrates that the method of finite spheres results are in good agreement with the analytical solutions for the two receivers on the surface.

An important point is here that all three waves with different wave speeds are quite accurately solved for. The reason is that we do not choose a time step size based on a CFL number (see Section 5.1.3).

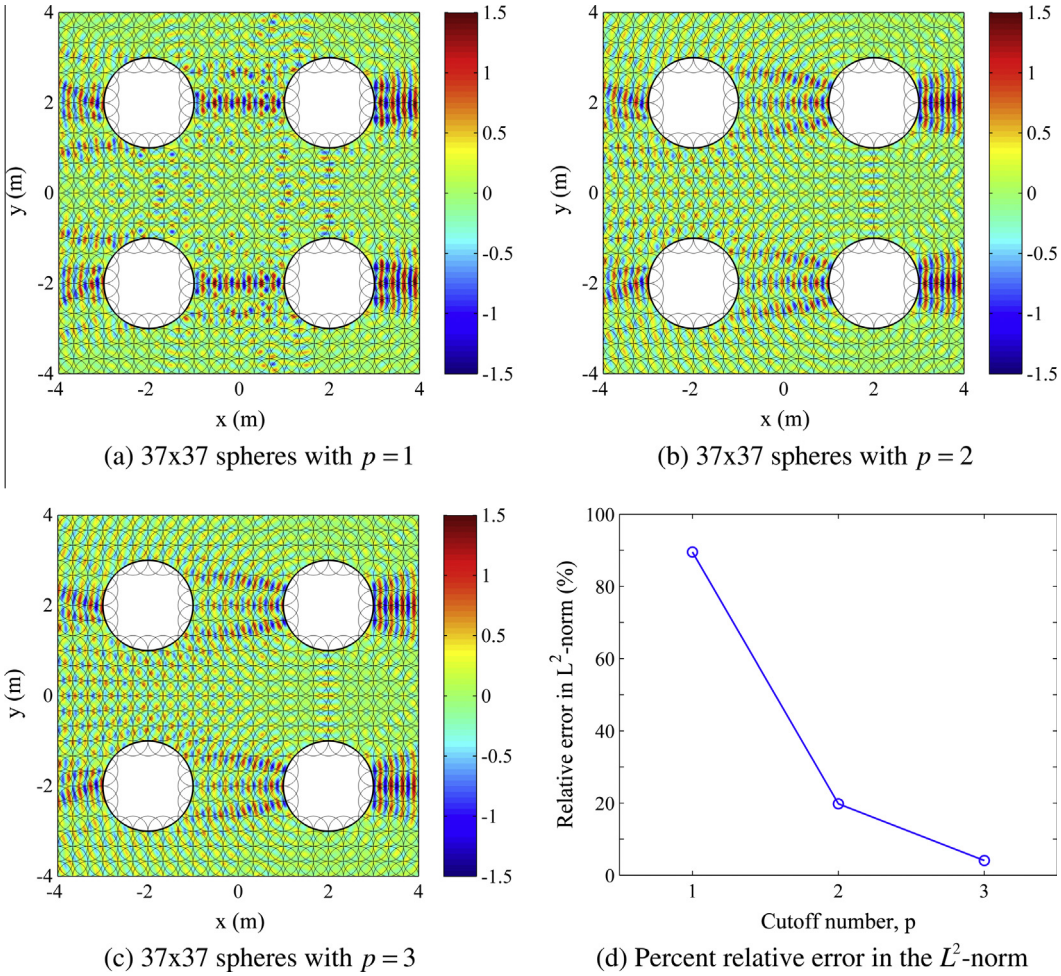

Fig. 12. Real part of numerical solution and percent relative error in the L^2-norm as a function of cutoff number.

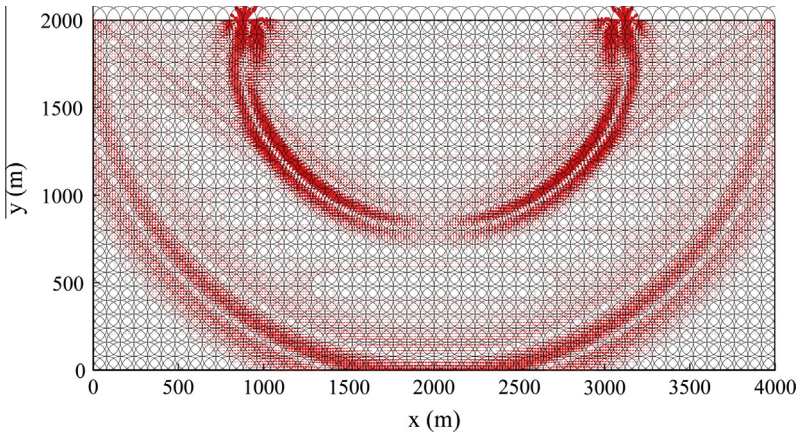

Fig. 13. Displacement field in semi-infinite elastic domain at $t = 0.74$ s.

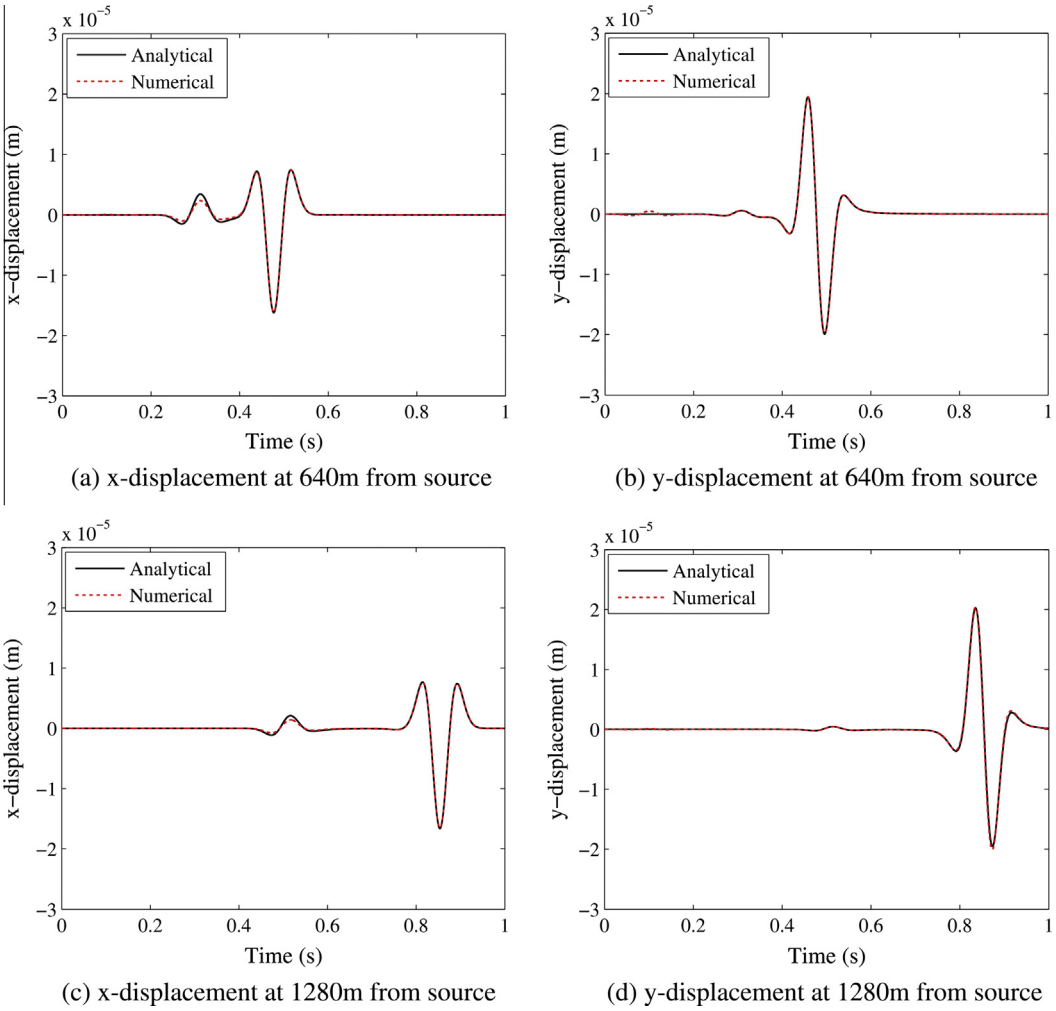

Fig. 14. Comparison between analytical and numerical solution for displacement variations at two locations.

5.4. Viscoelastic waves

Wave propagations in an actual body can be quite different from waves in an idealized linear elastic body due to friction effects. The viscous property in actual media causes dispersion and attenuation of the traveling waves [29–32].

Here we consider the wave propagations in a two-dimensional plane strain viscoelastic domain with a vertically applied Ricker wavelet at its center. The viscoelastic medium has P-wave velocity $v_p = 3000$ m/s, S-wave velocity $v_s = 2000$ m/s, and mass density $\rho = 2000$ kg/m^3. The domain size is 2000 m $\times$ 2000 m and the Ricker wavelet has magnitude 2×10^{10}, frequency $f = 50$ Hz, and time shift $t_0 = 0.06$ s. The spatial discretization is 33 $\times$ 33 spheres with cutoff number $p = 3$. The simulation duration is 0.5 s and the Bathe time integration method is used with time step size $\Delta t = 0.0004$ s. We use the quality factors $Q_p = 26$ for the P-wave attenuation and

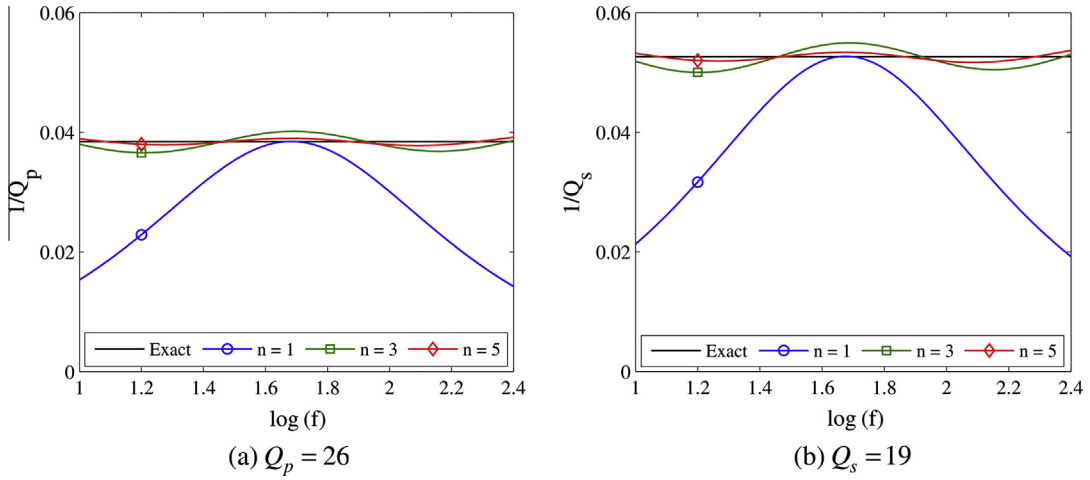

Fig. 15. Quality factors as a function of number of relaxation mechanisms.

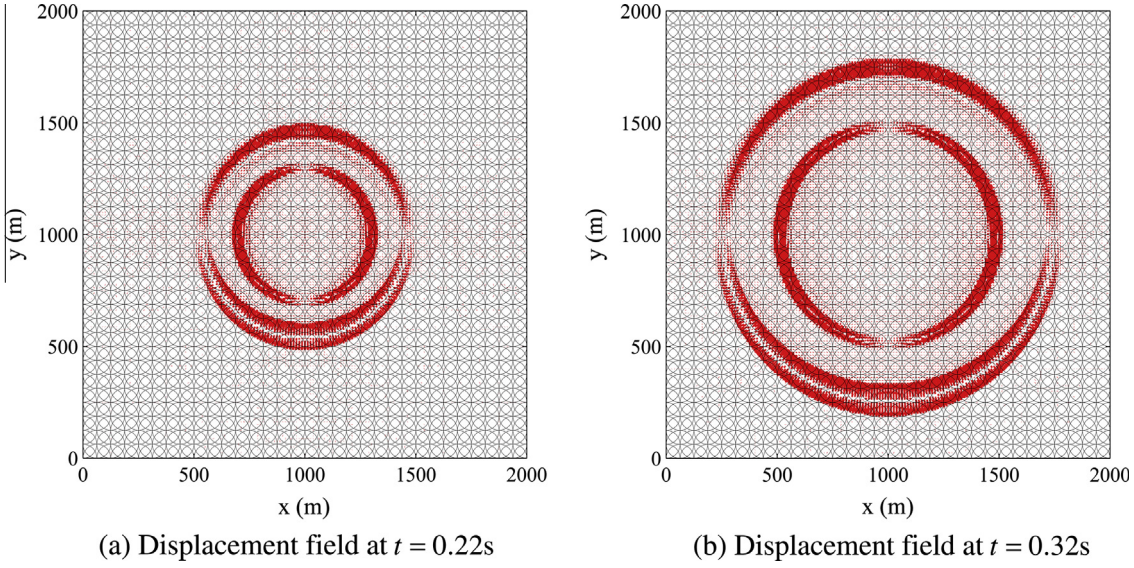

Fig. 16. Displacement field in viscoelastic medium.

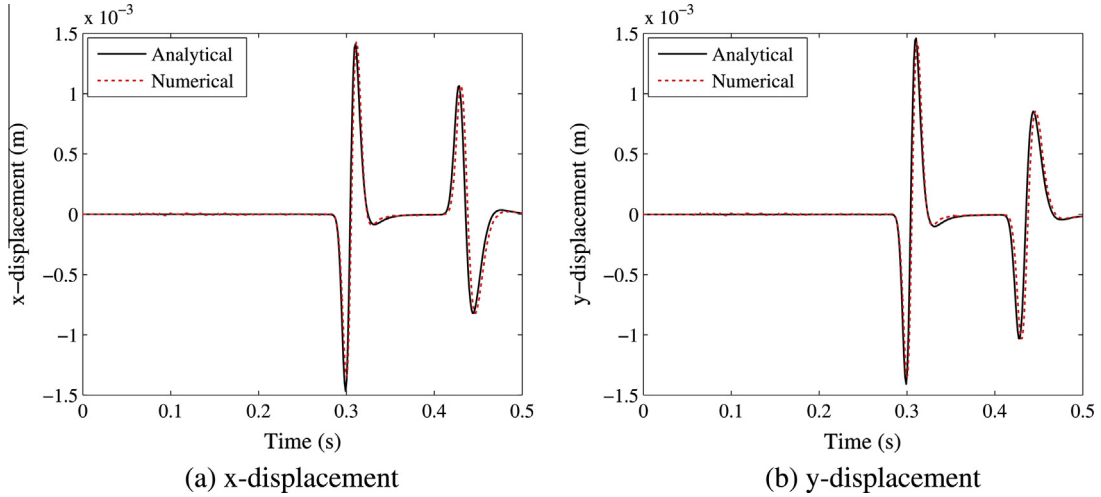

Fig. 17. Comparison between analytical and numerical solution for displacement variations at $(x, y) = (1500\text{ m}, 1500\text{ m})$.

$Q_s = 19$ for the S-wave attenuation. The analytical solution of this viscoelastic wave propagation problem can be obtained using Ref. [29].

Fig. 15 illustrates the approximations to the quality factors $1/Q_p$ and $1/Q_s$, for an increasing number of relaxation mechanisms using the generalized Maxwell model. As the number of relaxation mechanisms n increases, the error decreases, but the computational cost increases.

Fig. 16 shows the displacement fields in the viscoelastic body at $t = 0.22$ s and $t = 0.32$ s solved for when using $n = 3$. A comparison of the x- and y-displacement history at $(x, y) = (1500\text{ m}, 1500\text{ m})$ between the numerical and analytical solutions is shown in Fig. 17. We observe that the amplitude of the S-wave is smaller than of the P-wave due to a stronger attenuation of the S-wave. The method of finite spheres solution is in good agreement with the analytical solution.

6. Concluding remarks

The objective in this paper was to present in essence 'a finite element method with overlapping elements' – the method of finite spheres – for the solution of wave propagation problems. A main advantage of this formulation is that the solution is obtained without a mesh, avoiding discretization difficulties and element distortions.

With the method of finite spheres, the use of special interpolations for specific classes of problems is natural and we exploited this feature here using harmonic functions. A piecewise Gauss–Legendre quadrature rule was presented for the numerical integration. The reliability of the method was illustrated in the solution of some wave propagation problems, defined for elastic and viscoelastic media, by comparison with the analytical solutions.

However, while the results given in the paper are valuable, there is much further research to be performed regarding the method. We used in this paper only equal size spheres (or rather disks) and only solved problems involving simple geometries. It should still be investigated how the procedure performs when complex geometries are considered and non-equal size spheres are employed. In these studies also the condition numbers of the matrices employed in the solutions need to be considered, since these might grow due to the use of different sizes of spheres [8] and the use of harmonic functions [9]. Furthermore, the numerical integration scheme employed should be analyzed deeply. Such analysis might result in a more effective scheme.

An advantage that we observed with the method is that the use of smaller size time steps leads to more accurate solutions. Hence an optimal CFL number is not used, and multiple waves traveling through media can be accurately simulated. However, a deeper investigation in the choice of a "best" time step size using the Bathe method and also other implicit time integration schemes would be valuable.

Although only two-dimensional problems have been considered, the method of finite spheres can, theoretically, directly be extended to the solution of three-dimensional problems. Indeed, it is in the solution of three-dimensional problems where good finite element meshes, without highly distorted elements, are difficult to reach.

However, the first step might then be to first identify whether the method of finite spheres with the integration scheme proposed in this paper (or a more effective one) is indeed competitive in the solution of three-dimensional linear static problems, when compared to the use of the finite element method. In such study, also the use of parallel processing should be included. Thereafter, the solution of three-dimensional wave propagation problems might be tackled, where instead of implicit integration, like using the Bathe method in this paper, also explicit time integration should be explored, like using the Noh-Bathe scheme [40].

Hence, altogether, many research topics still exist regarding the method of (overlapping) finite spheres, where indeed the words "overlapping finite spheres" should be interpreted in a more general sense as "overlapping finite simple domains". For example, also the use of square domains and equal-faced bricks in two- and three-dimensional analyses, respectively, might be valuable.

References

[1] De S, Bathe KJ. The method of finite spheres. Comput Mech 2000;25:329–45.
[2] De S, Bathe KJ. Displacement/pressure mixed interpolation in the method of finite spheres. Int J Numer Meth Eng 2001;51:275–92.
[3] De S, Bathe KJ. The method of finite spheres with improved numerical integration. Comput Struct 2001;79:2183–96.
[4] Hong JW, Bathe KJ. Coupling and enrichment schemes for finite element and finite sphere discretizations. Comput Struct 2005;83:1386–95.
[5] Macri M, De S. Towards an automatic discretization scheme for the method of finite spheres and its coupling with the finite element method. Comput Struct 2005;83:1429–47.
[6] Macri M, De S. Enrichment of the method of finite spheres using geometry-independent localized scalable bubbles. Int J Numer Meth Eng 2007;69:1–32.
[7] Liu GR. Mesh free methods: moving beyond the finite element method. CRC Press; 2003.
[8] Bathe KJ. Finite element procedures. Prentice Hall; 1996.
[9] Ham S, Bathe KJ. A finite element method enriched for wave propagation problems. Comput Struct 2012;94–95:1–12.
[10] Bathe KJ, Noh G. Insight into an implicit time integration scheme for structural dynamics. Comput Struct 2012;98–99:1–6.
[11] Noh G, Ham S, Bathe KJ. Performance of an implicit time integration scheme in the analysis of wave propagations. Comput Struct 2013;123:93–105.
[12] Ihlenburg F, Babuška I. Finite element solution of the Helmholtz equation with high wave number. Part 1: the h-version of the FEM. Comput Math Appl 1995;30:9–37.
[13] Petersen S, Dreyer D, von Estorff O. Assessment of finite and spectral element shape functions for efficient iterative simulations of interior acoustics. Comput Method Appl M 2006;195:6463–78.
[14] Komatitsch D, Vilotte JP. The spectral element method: an efficient tool to simulate the seismic response of 2D and 3D geological structures. Bull Seismol Soc Am 1998;88:368–92.
[15] Pasquetti R, Rapetti F. Spectral element methods on triangles and quadrilaterals: comparisons and applications. J Comput Phys 2004;198:349–62.
[16] Liu MB, Liu GR. Smoothed particle hydrodynamics (SPH): an overview and recent developments. Arch Comput Methods Eng 2010;17:25–76.
[17] Herreros MI, Mabssout M. A two-steps time discretization scheme using the SPH method for shock wave propagation. Comput Method Appl M 2011;200:1833–45.
[18] Belytschko T, Lu YY, Gu L. Element-free Galerkin methods. Int J Numer Meth Eng 1994;37:229–56.
[19] Jia XF, Hu TY. Element-free precise integration method and its applications in seismic modeling and imaging. Geophys J Int 2006;166:349–72.
[20] Atluri SN, Kim HG, Cho JY. A critical assessment of the truly meshless local Petrov-Galerkin (MLPG), and local boundary integral equation (LBIE) methods. Comput Mech 1999;24:348–72.
[21] Soares D. Numerical modelling of electromagnetic wave propagation by meshless local Petrov-Galerkin formulations. CMES-Comput Model Eng 2009;50:97–114.
[22] Nicomedes WL, Mesquita RC, Moreira FJS. The meshless local Petrov-Galerkin method in two-dimensional electromagnetic wave analysis. IEEE Trans Antenn Propag 2012;60:1957–68.
[23] Wen PH. Meshless local Petrov-Galerkin (MLPG) method for wave propagation in 3D poroelastic solids. Eng Anal Bound Elem 2010;34:315–23.
[24] Godinho L, Dors C, Soares D, Amado-Mendes P. Solution of time-domain acoustic wave propagation problems using a RBF interpolation model with "a priori" estimation of the free parameter. Wave Motion 2011;48:423–40.
[25] Wong ASM, Hon YC, Li TS, Chung SL, Kansa EJ. Multizone decomposition for simulation of time-dependent problems using the multiquadric scheme. Comput Math Appl 1999;37:23–43.
[26] Sarra SA, Sturgill D. A random variable shape parameter strategy for radial basis function approximation methods. Eng Anal Bound Elem 2009;33:1239–45.
[27] Duarte CA, Oden JT. An h–p adaptive method using clouds. Comput Method Appl M 1996;139:237–62.
[28] Melenk JM, Babuška I. The partition of unity finite element method: basic theory and applications. Comput Method Appl M 1996;139:289–314.
[29] Carcione JM, Kosloff D, Kosloff R. Wave propagation simulation in a linear viscoelastic medium. Geophys J 1988;95:597–611.
[30] Lombard B, Piraux J. Numerical modeling of transient two-dimensional viscoelastic waves. J Comput Phys 2011;230:6099–114.

[31] Kristek J, Moczo P. Seismic-wave propagation in viscoelastic media with material discontinuities: a 3D fourth-order staggered-grid finite-difference modeling. Bull Seismol Soc Am 2003;93:2273–80.
[32] Moczo P, Kristek J, Galis M, Pazak P, Balazovjech M. The finite-difference and finite-element modeling of seismic wave propagation and earthquake motion. Acta Phys Slovaca 2007;57:177–406.
[33] Mazzia A, Ferronato M, Pini G. A comparison of numerical integration rules for the meshless local Petrov-Galerkin method. Numer Algorithms 2007;45:61–74.
[34] Liu Y, Belytschko T. A new support integration scheme for the weakform in mesh-free methods. Int J Numer Meth Eng 2010;82:699–715.
[35] Grätsch T, Bathe KJ. A posteriori error estimation techniques in practical finite element analysis. Comput Struct 2005;83:235–65.
[36] Yue B, Guddati MN. Dispersion-reducing finite elements for transient acoustics. J Acoust Soc Am 2005;118:2132–41.
[37] Bathe KJ, Wilson EL. Stability and accuracy analysis of direct integration methods. Earthquake Eng Struct 1973;1:283–91.
[38] Mohamed MS, Laghrouche O, El-Kacimi A. Some numerical aspects of the PUFEM for efficient solution of 2D Helmholtz problems. Comput Struct 2010;88:1484–91.
[39] Linton CM, Evans DV. The interaction of waves with arrays of vertical circular-cylinders. J Fluid Mech 1990;215:549–69.
[40] Noh G, Bathe KJ. An explicit time integration scheme for the analysis of wave propagations. Comput Struct 2013;129:178–93.